Supplement of Atmos. Chem. Phys., 21, 17243–17265, 2021
https://doi.org/10.5194/acp-21-17243-2021-supplement

Supplement of

Reduced effective radiative forcing from cloud–aerosol interactions (ERF_{aci}) with improved treatment of early aerosol growth in an Earth system model

Sara Marie Blichner et al.

Correspondence to: Sara Marie Blichner (s.m.blichner@geo.uio.no)

1 Sensitivity to nucleation parameterization

In order to test the sensitivity of our results to the nucleation parameterization, we ran additional simulations where this was changed. We added the temperature dependency presented in Yu et al. (2017) and we also ran the sectional scheme with the same nucleation parameterization as OsloAero$_{def}$, namely eq. 18 from Paasonen et al. (2010). In total this constitutes these additional model runs:

1. OsloAero$_{depT}$: The same as OsloAero$_{imp}$, but with a temperature dependency on the nucleation rate from Yu et al. (2017).

2. OsloAeroSec$_{depT}$: The same as OsloAeroSec, but with a temperature dependency on the nucleation rate from Yu et al. (2017).

3. OsloAeroSec$_{paas}$: The same as OsloAeroSec, but with the nucleation rate from Paasonen et al. (2010), i.e. the same as in OsloAero$_{def}$.

The results for ERF from aerosols are shown in Fig. S1 (which is analogous to Fig. 3 in the main text) and Fig. S2 (analogous to Fig. 4 in the main text). Figure S1 shows that the change in ERF$_{aci}$ between the sectional and default model is resistant to changes in nucleation rate. There are small differences within the OsloAero model versions and within the OsloAeroSec versions, but larger differences between the two groups.

2 Extra model evaluation

The model versions used in this paper were evaluated thoroughly in Blichner et al. (2021). However, we here supplement this evaluation with three locations that were not covered in the previous paper. We have compared our data against NASA Atmospheric Tomography Mission (ATom) aircraft measurements (Wofsy et al., 2018), measurements at the Amazon Tall

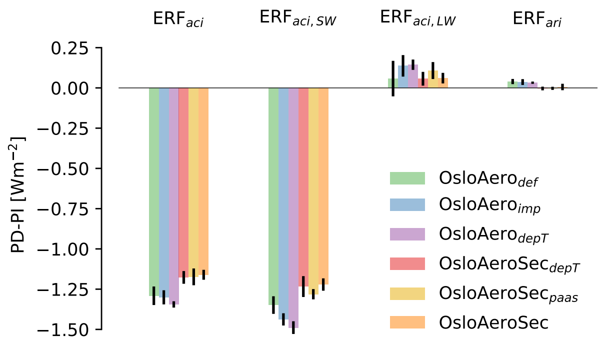

Figure S1. Globally averaged effective radiative forcings (ERF) from aerosols. ERF$_{aci}$ is the ERF from aerosol-cloud interaction, ERF$_{aci,SW}$ and ERF$_{aci,LW}$ are the short wave and long wave component of ERF$_{aci}$ and ERF$_{ari}$ is the ERF from aerosol radiation interaction alone. All are computed in accordance with Ghan (2013). The circles are the the averages for each individual year in the 5 year simulations and the gray bar indicates the 95% confidence interval of the mean.

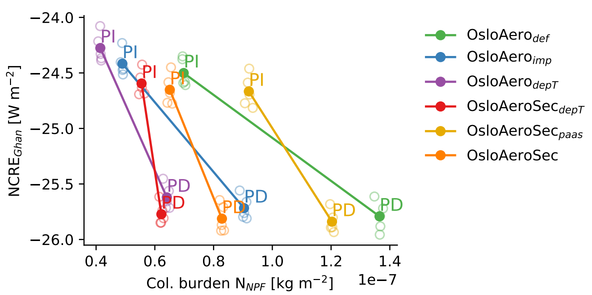

Figure S2. Globally averaged aerosol values of NCRE$_{Ghan}$ (y-axis) and column burden of NPF particles (x-axis) for the pre-industrial (PI) and present day (PD) atmosphere. The circles show each annual average and are included to indicate the variability.

Tower Observatory (ATTO, 02° 08.752'S, 59° 00.335'W, Andreae et al. (2015)), and measurements at Mount Chacataya (CHC, 16°21.014'S, 68°07.886'W, 5240 meters above sea level, Andrade et al. (2015), see also Bianchi et al. (2021) for site description). These locations were chosen because they supplement the previous evaluation by being located in very different environments (southern hemisphere, high altitude, aircraft measurements).

2.1 Method

We use the model output as described in Blichner et al. (2021) for these validations. The model versions are the same as in this study. The resolution is the same as in this study: 1.9° (latitude) $\times$ 2.5° (longitude) resolution grid with 32 height levels from the surface to $\sim$2.2 hPa in hybrid sigma coordinates. We used prescribed sea surface temperature (SST) and sea ice concentrations (Hurrell et al., 2008). The simulations were run from 2007 and throughout 2014 with CMIP6 historical emissions and greenhouse gas concentrations (Seland et al., 2020) and the meteorology (horizontal wind and surface pressure) is nudged to ERA-Interim (Berrisford et al., 2011) using a relaxation time of 6 hours (Kooperman et al., 2012) (as described in Karset (2020, sec 4.1)). All years from 2008–2014 were included in the comparison below, while year 2007 was discarded as spin-up. The output used in the following analysis is monthly means.

2.1.1 ATom

The data was accessed from https://daac.ornl.gov/ATOM/guides/ATom_merge.html (last accessed: 2021-06-20) and includes measurements of particle number in the nucleation mode (down to 2.7 nm), Aitken mode, accumulation mode and coarse mode from four aircraft campaigns, taken at 4 different times of year and each ranging almost pole to pole and focusing on the remote Pacific and Atlantic oceans (WOFSY and Team, 2018; Wofsy et al., 2018).

To make as fair a comparison as possible, we first categorize which grid box in the model each measurement would fall within. We then average over all the values in each grid box so that we get a gridded observational dataset on the same grid as the model. Finally, we mask the model output so that we only consider the grid boxes where we have observations in the following comparison.

Note that the resolution of the model output is monthly means, and thus the time dimension is only considered in the selection of the most relevant month of the year (ATom 1: 2016-07-29–2016-08-23 $\rightarrow$ August, ATom 2: 2017-01-26 to 2017-02-21 $\rightarrow$ February, ATom 3: 2017-09-28 to 2017-10-28 $\rightarrow$ October, ATom 4: 2018-04-24 to 2018-05-21 $\rightarrow$ May).

For the comparison, we use the number of particles above 60 nm, N_{60}, which is both available from the ATom data and a good indicator of the number of CCN relevant particles.

2.1.2 ATTO tower and Mount Chacataya

We use size distribution data from both these stations. The data from Chacataya is available for download from the EBAS database (http://ebas.nilu.no/Pages/DataSetList.aspx?key=24F2E44259AE4E089EC74128B761A2F8, last accessed 2021-08-15), while the data from ATTO tower was downloaded from the Laboratory of Atmospheric Physics (LFA, IF-USP)) http://ftp.lfa.if.usp.br/ftp/public/LFA_Processed_Data/T0a_ATTO/Level3/SMPS_2014toNov2020_ATTO_60m_InstTower/, last accessed 2021-08-15).

The data from CHC covers the years 2012–2019, while the ATTO dataset covers 2014–2019. There are some missing data, so to overcome this, we first create a monthly average of the size distribution, and then average over the months. This has negligible impact on the resulting average compared to doing an average over all the values.

For the ATTO tower, we use the bottom layer of the model, consistent approximately with the height of the measurement point (60 m). For CHC it is more unclear what would be the appropriate model level, because the grid of the model is so coarse that the geopotential height of the bottom layer of the grid box is only a little over 2100 meters above sea level (masl). This illustrates well the difficulty of validation of an ESM against measurement stations in complex terrain environments – choosing the bottom layer may be inappropriate for obvious reasons, but choosing a layer too far from the modelled ground may be inappropriate due to lack of modelled influence from the surface (boundary layer influence e.g.). As a compromise, we average over the grid boxes that are from approximately 3000 to 5000 masl in geopotential height.

2.2 Results

2.2.1 ATom

Comparisons against each of the ATom campaigns for N_{60} are shown in Fig. S3 for different latitude ranges. Mostly it is hard to draw conclusions about which model is better, because the difference between the models is often considerably smaller than the difference to the measurement. All model versions underestimate the number of particles in the upper troposphere in the tropics. Some improvement can be seen with OsloAeroSec in some tropical areas, like 30–0 °S for ATom 2 and 4. In Antarctica and the Southern Ocean the models seems to perform more or less the same. In 30–60 °N, OsloAeroSec shows some improvement compared to the others in ATom-1 and 2 (August and February), while the opposite is the case for ATom-3 and 4 (September and May). Finally in 60–90 °N, the models often underestimate the number of particles and OsloAero$_{def}$ performs better than the others in ATom-3 and ATom-4. These results overall suggest a lack of particles in the modelled upper troposphere, which is consistent with the findings of Williamson et al. (2019) for other ESMs as well. Going in detail on why this might be is outside the scope of this study, but possible reasons could be missing nucleation mechanisms (outside the boundary layer, the models currently includes only sulfuric acid–water nucleation) and, as suggested by Williamson et al. (2019), excessive wet removal by cloud processing.

2.2.2 ATTO tower

The modelled size distribution throughout the year is compared to the measured one in Fig. S4 and the annual average is shown in Fig. S6. Note that the size distribution from the model is generated from monthly means of the log-normal mode parameters, namely the number, standard deviation σ and number median diameter of each mode. This may result in some unrealistic narrowing of the modes. Overall, it is clear that all the models have distributions which are too narrow and that number concentrations are too high. While the observed size distribution shows little sign of NPF, NPF is present in all model versions. However, the change in nucleation parameterization from OsloAero$_{def}$ to OsloAero$_{imp}$ and OsloAeroSec has clearly reduced NPF and thus increased the realism of the model.

2.2.3 Mount Chacataya station

The modelled size distribution throughout the year is compared to the measured one in Fig. S5 and the annual average is shown in the left panel og Fig. S6. Contrary to the ATTO station, these results show an underestimation of the smallest particles. However, in the sizes above approximately 100 nm, the models overestimate the concentration. The overestimation is particularly high for OsloAero$_{def}$. These differences may be due to underestimation of the nucleation rate and/or an overestimation of growth rates, thus shifting the particles to larger sizes.

References

Andrade, M., Zaratti, F., Forno, R., Gutiérrez, R., Moreno, I., Velarde, F., Ávila, F., Roca, M., Sánchez, M. F., Laj, P., Jaffrezo, J. L., Ginot, P., Sellegri, K., Ramonet, M., Laurent, O., Weinhold, K., Wiedensohler, A., Krejci, R., Bonasoni, P., Cristofanelli, P., Whiteman, D., Vimeux, F., Dommergue, A., and Magand, O.: Puesta En Marcha de Una Nueva Estación de Monitoreo Climático En Los Andes Centrales de Bolivia: La Estación Gaw/Chacaltaya, Revista Boliviana de Física, 26, 06–15, 2015.

Andreae, M. O., Acevedo, O. C., Araùjo, A., Artaxo, P., Barbosa, C. G. G., Barbosa, H. M. J., Brito, J., Carbone, S., Chi, X., Cintra, B. B. L., da Silva, N. F., Dias, N. L., Dias-Júnior, C. Q., Ditas, F., Ditz, R., Godoi, A. F. L., Godoi, R. H. M., Heimann, M., Hoffmann, T., Kesselmeier, J., Könemann, T., Krüger, M. L., Lavric, J. V., Manzi, A. O., Lopes, A. P., Martins, D. L., Mikhailov, E. F., Moran-Zuloaga, D., Nelson, B. W., Nölscher, A. C., Santos Nogueira, D., Piedade, M. T. F., Pöhlker, C., Pöschl, U., Quesada, C. A., Rizzo, L. V., Ro, C.-U., Ruckteschler, N., Sá, L. D. A., de Oliveira Sá, M., Sales, C. B., dos Santos, R. M. N., Saturno, J., Schöngart, J., Sörgel, M., de Souza, C. M., de Souza, R. a. F., Su, H., Targhetta, N., Tóta, J., Trebs, I., Trumbore, S., van Eijck, A., Walter, D., Wang, Z., Weber, B., Williams, J., Winderlich, J., Wittmann, F., Wolff, S., and Yáñez-Serrano, A. M.: The Amazon Tall Tower Observatory (ATTO): Overview of Pilot Measurements on Ecosystem Ecology, Meteorology, Trace Gases, and Aerosols, Atmospheric Chemistry and Physics, 15, 10 723–10 776, https://doi.org/10.5194/acp-15-10723-2015, 2015.

Berrisford, P., Dee, D., Poli, P., Brugge, R., Fielding, M., Fuentes, M., Kållberg, P., Kobayashi, S., Uppala, S., and Simmons, A.: The ERA-Interim Archive Version 2.0, p. 23, 2011.

Bianchi, F., Sinclair, V. A., Aliaga, D., Zha, Q., Scholz, W., Wu, C., Heikkinen, L., Modini, R., Partoll, E., Velarde, F., Moreno, I., Gramlich, Y., Huang, W., Leiminger, M., Enroth, J., Peräkylä, O., Marinoni, A., Xuemeng, C., Blacutt, L., Forno, R., Gutierrez, R., Ginot, P., Uzu, G., Facchini, M. C., Gilardoni, S., Gysel-Beer, M., Cai, R., Petäjä, T., Rinaldi, M., Saathoff, H., Sellegri, K., Worsnop, D., Artaxo, P., Hansel, A., Kulmala, M., Wiedensohler, A., Laj, P., Krejci, R., Carbone, S., Andrade, M., and Mohr, C.: The SALTENA Experiment: Comprehensive Observations of Aerosol Sources, Formation and Processes in the South American Andes, Bulletin of the American Meteorological Society, -1, 1–46, https://doi.org/10.1175/BAMS-D-20-0187.1, 2021.

Blichner, S. M., Sporre, M. K., Makkonen, R., and Berntsen, T. K.: Implementing a Sectional Scheme for Early Aerosol Growth from New Particle Formation in the Norwegian Earth System Model v2: Comparison to Observations and Climate Impacts, Geoscientific Model Development, 14, 3335–3359, https://doi.org/10.5194/gmd-14-3335-2021, 2021.

Ghan, S. J.: Technical Note: Estimating Aerosol Effects on Cloud Radiative Forcing, Atmos. Chem. Phys., 13, 9971–9974, https://doi.org/10.5194/acp-13-9971-2013, 2013.

Hurrell, J. W., Hack, J. J., Shea, D., Caron, J. M., and Rosinski, J.: A New Sea Surface Temperature and Sea Ice Boundary Dataset for the Community Atmosphere Model, Journal of Climate, 21, 5145–5153, https://doi.org/10.1175/2008JCLI2292.1, 2008.

Karset, I. H. H.: Enhancing the Confidence in Estimates of Effective Radiative Forcing by Aerosol through Improved Global Modelling, Ph.D. thesis, University of Oslo, Oslo, 2020.

Kooperman, G. J., Pritchard, M. S., Ghan, S. J., Wang, M., Somerville, R. C. J., and Russell, L. M.: Constraining the Influence of Natural Variability to Improve Estimates of Global Aerosol Indirect Effects in a Nudged Version of the Community Atmosphere Model 5, Journal of Geophysical Research: Atmospheres, 117, https://doi.org/10.1029/2012JD018588, 2012.

Paasonen, P., Nieminen, T., Asmi, E., Manninen, H. E., Petäjä, T., Plass-Dülmer, C., Flentje, H., Birmili, W., Wiedensohler, A., Hõrrak, U., Metzger, A., Hamed, A., Laaksonen, A., Facchini, M. C., Kerminen, V.-M., and Kulmala, M.: On the Roles of Sulphuric Acid and

Low-Volatility Organic Vapours in the Initial Steps of Atmospheric New Particle Formation, Atmos. Chem. Phys., 10, 11 223–11 242, https://doi.org/10.5194/acp-10-11223-2010, 2010.

Seland, Ø., Bentsen, M., Seland Graff, L., Olivié, D., Toniazzo, T., Gjermundsen, A., Debernard, J. B., Gupta, A. K., He, Y., Kirkevåg, A., Schwinger, J., Tjiputra, J., Schancke Aas, K., Bethke, I., Fan, Y., Griesfeller, J., Grini, A., Guo, C., Ilicak, M., Hafsahl Karset, I. H., Landgren, O., Liakka, J., Onsum Moseid, K., Nummelin, A., Spensberger, C., Tang, H., Zhang, Z., Heinze, C., Iverson, T., and Schulz, M.: The Norwegian Earth System Model, NorESM2 – Evaluation of theCMIP6 DECK and Historical Simulations, Geoscientific Model Development Discussions, pp. 1–68, https://doi.org/10.5194/gmd-2019-378, 2020.

Williamson, C. J., Kupc, A., Axisa, D., Bilsback, K. R., Bui, T., Campuzano-Jost, P., Dollner, M., Froyd, K. D., Hodshire, A. L., Jimenez, J. L., Kodros, J. K., Luo, G., Murphy, D. M., Nault, B. A., Ray, E. A., Weinzierl, B., Wilson, J. C., Yu, F., Yu, P., Pierce, J. R., and Brock, C. A.: A Large Source of Cloud Condensation Nuclei from New Particle Formation in the Tropics, Nature, 574, 399–403, https://doi.org/10.1038/s41586-019-1638-9, 2019.

WOFSY, S. and Team, A. S.: ATom: Aircraft Flight Track and Navigational Data, p. 200.237798 MB, https://doi.org/10.3334/ORNLDAAC/1613, 2018.

Wofsy, S., Afshar, S., Allen, H., Apel, E., Asher, E., Barletta, B., Bent, J., Bian, H., Biggs, B., Blake, D., Blake, N., Bourgeois, I., Brock, C., Brune, W., Budney, J., Bui, T., Butler, A., Campuzano-Jost, P., Chang, C., Chin, M., Commane, R., Correa, G., Crounse, J., Cullis, P. D., Daube, B., Day, D., Dean-Day, J.M., Dibb, J., DiGangi, J., Diskin, G., Dollner, M., Elkins, J., Erdesz, F., Fiore, A., Flynn, C., Froyd, K., Gesler, D., Hall, S., Hanisco, T., Hannun, R., Hills, A., Hintsa, E., Hoffman, A., Hornbrook, R., Huey, L., Hughes, S., Jimenez, J., Johnson, B., Katich, J., Keeling, R., Kim, M., Kupc, A., Lait, L., Lamarque, J.-F., Liu, J., McKain, K., Mclaughlin, R., Meinardi, S., Miller, D., Montzka, S., Moore, F., Morgan, E., Murphy, D., Murray, L., Nault, B., Neuman, J., Newman, P., Nicely, J., Pan, X., Paplawsky, W., Peischl, J., Prather, M., Price, D., Ray, E., Reeves, J., Richardson, M., Rollins, A., Rosenlof, K., Ryerson, T., Scheuer, E., Schill, G., Schroder, J., Schwarz, J., St.Clair, J., Steenrod, S., Stephens, B., Strode, S., Sweeney, C., Tanner, D., Teng, A., Thames, A., Thompson, C., Ullmann, K., Veres, P., Vieznor, N., Wagner, N., Watt, A., Weber, R., Weinzierl, B., Wennberg, P., Williamson, C., Wilson, J., Wolfe, G., Woods, C., and Zeng, L.: Atmospheric Tomography Mission (ATom)ATom: Merged Atmospheric Chemistry, Trace Gases, and Aerosols, p. 0 MB, https://doi.org/10.3334/ORNLDAAC/1581, 2018.

Yu, F., Luo, G., Nadykto, A. B., and Herb, J.: Impact of Temperature Dependence on the Possible Contribution of Organics to New Particle Formation in the Atmosphere, Atmospheric Chemistry and Physics, 17, 4997–5005, https://doi.org/10.5194/acp-17-4997-2017, 2017.

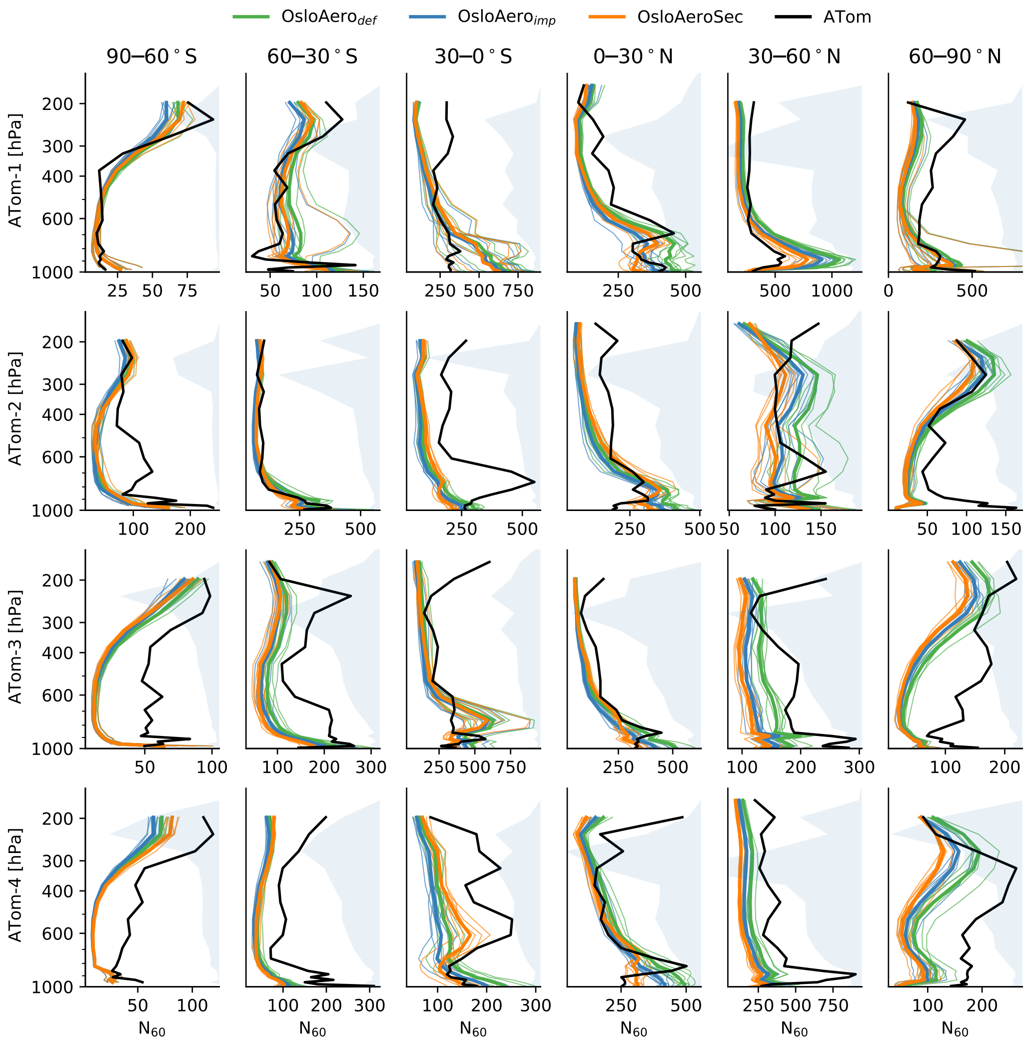

Figure S3. Average over time, longitude and latitude for model (after masking for observational cover) and measurements from the different ATom campaigns. Each column shows the average over a latitude band (90–60°S, 60–30°S, 30–0°S, 0–30°N, 30–60°N, 60–90°N). Each weak line is the relevant month of one year of the simulations (2008-2014) and the thicker line is the mean of all of these. We use monthly mean data from the models and thus choose the month which is covered by the measurement campaign. For the observations, we pick out the grid boxes covered by the flight campaign and average the measurements within one model grid-box, thus creating a dataset similar to the model. Both model data and observations are finally averaged, weighted by the grid box area. The shading shows the number of measurements done in each height level, thus indicating how well sampled each height is.

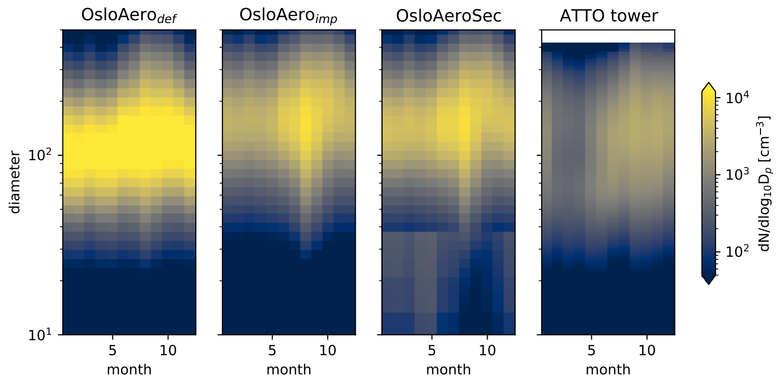

Figure S4. Annual variability in the particle number size distributions of models (first 3 columns) and in measurements (last column) at the ATTO tower shown by monthly averages.

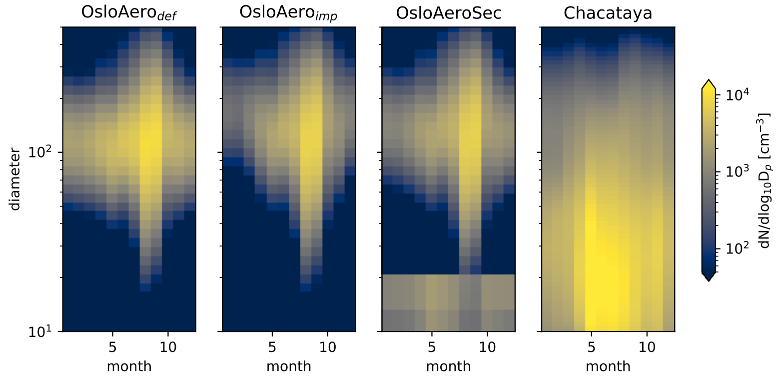

Figure S5. Annual variability in the particle number size distributions of models (first 3 columns) and in measurements (last column) at Mount Chacataya shown by monthly averages.

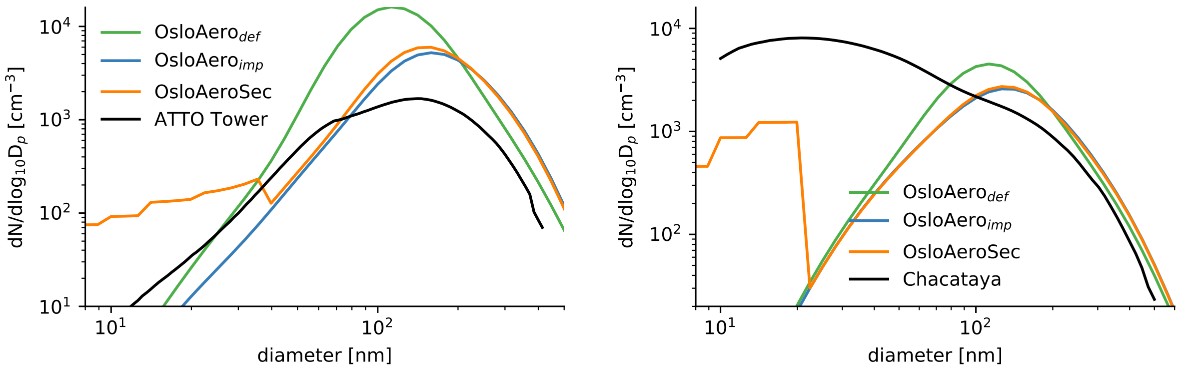

Figure S6. Modelled and observed particle number size distributions for the ATTO tower (left) and Mount Chacataya (right).

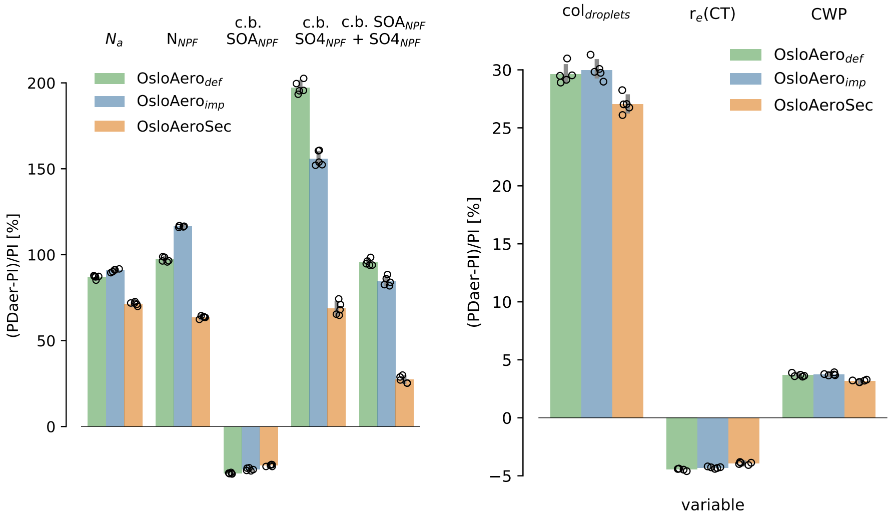

Figure S7. Globally averaged change in aerosol and cloud properties. N$_a$: total number of particles, N$_{NPF}$: number of particles from NPF, c.b. SOA$_{NPF}$: column burden of SOA in NPF particles, i.e which has been part of the growth up to the modal scheme, c.b. SO4$_{NPF}$: column burden of SO4 in NPF particles, i.e which has been part of the growth up to the modal scheme, c.b. SOA$_{NPF}$+SO4$_{NPF}$: sum of the two previous, col$_{droplets}$: the column integrated number of cloud droplets, r_e(CT): effective radius of cloud droplets at cloud top, CWP: cloud water path. N$_{NPF}$ and N$_a$ values are averaged up to 850 hPa and weighted by pressure difference of the grid cell.

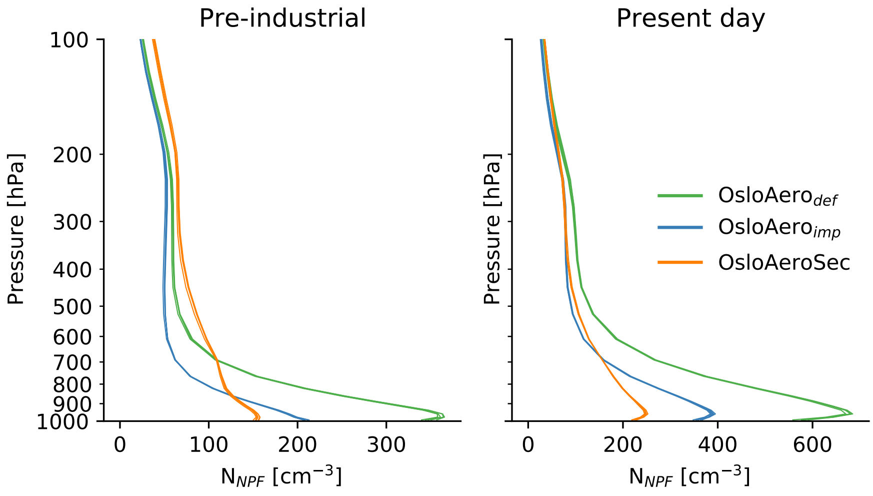

Figure S8. Globally averaged concentration of aerosols from NPF for pre-industrial (left) and present day (right) aerosols. The individual lines represent the annual average of each year in each simulation.

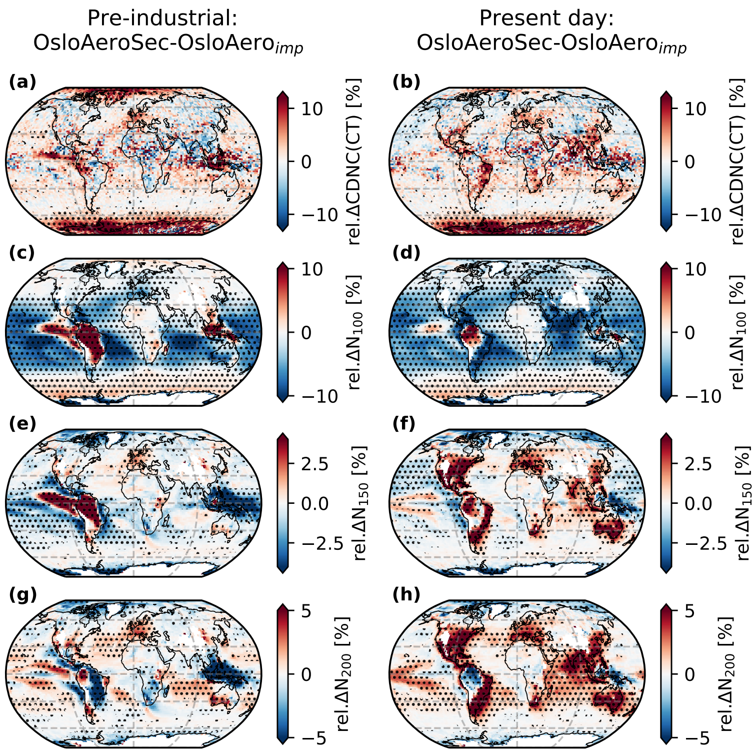

Figure S9. Top row: Difference in average cloud droplet number concentrations (CDNC) at cloud top between OsloAeroSec and OsloAero$_{def}$. Row 2–3: difference in average particle number concentration for particles larger than 100 nm (row 2), 150 nm (row 3) and 200 nm (row 4). The left column shows the difference for the pre-industrial atmosphere and the right column shows the difference for the present day atmosphere. The average particle concentrations are calculated averaging up to 850 hPa and averaging by pressure difference. Dots are included in the plots to indicate where the difference between the two models is significant with a two-tailed paired Student's t–test with 95 % confidence interval.

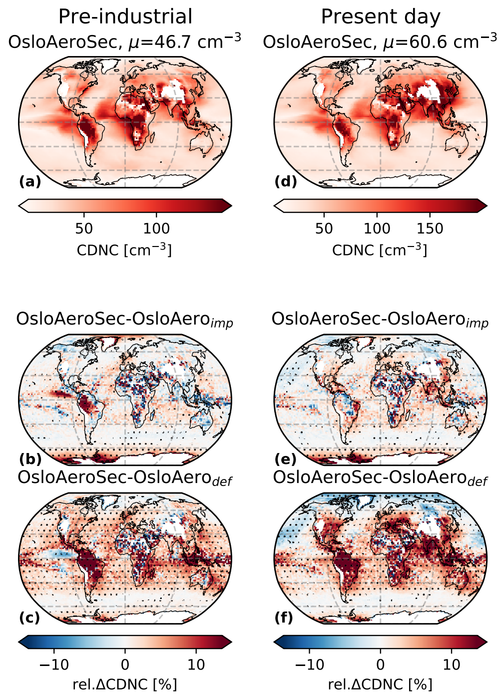

Figure S10. Top row: Near surface CDNC in OsloAeroSec for PI and PD atmosphere. Row 2 and 3 show the difference between OsloAeroSec and OsloAero$_{imp}$ and OsloAero$_{def}$ respectively. The average is calculated for grid boxes up to 850 hPa and averaging by pressure difference. Dots are included in the plots to indicate where the difference between the two models is significant with a two-tailed paired Student's t–test with 95 % confidence interval.

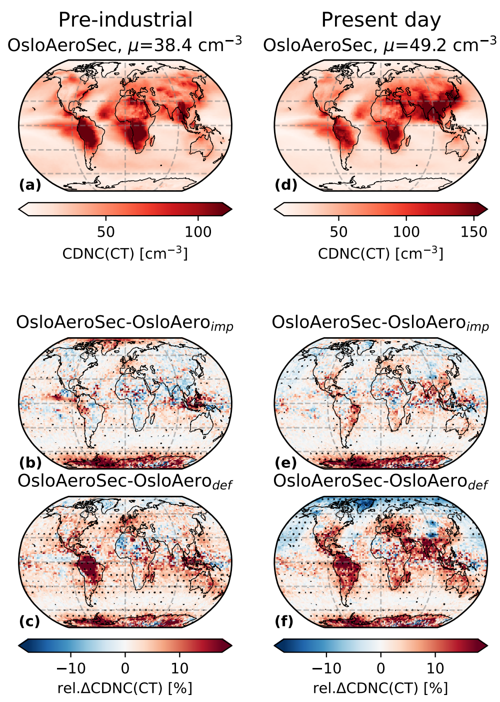

Figure S11. Top row: Cloud top CDNC in OsloAeroSec for PI and PD atmosphere. Row 2 and 3 show the difference between OsloAeroSec and OsloAero$_{imp}$ and OsloAero$_{def}$ respectively.

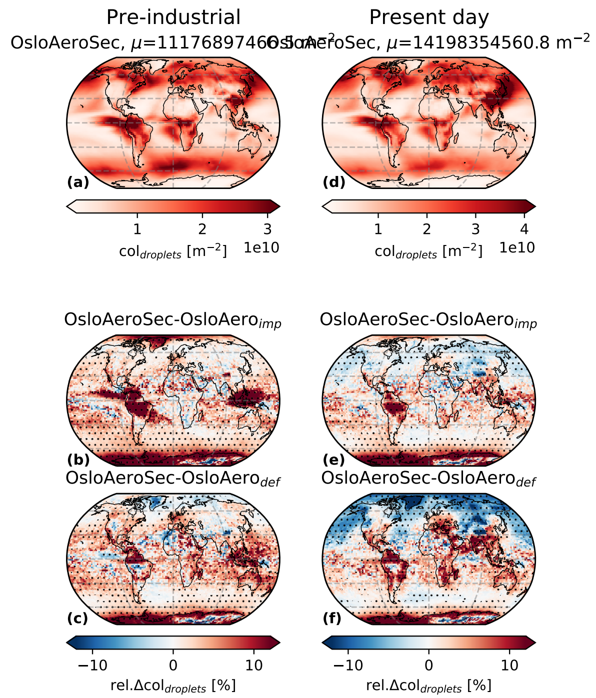

Figure S12. Top row: Column integrated droplet number in OsloAeroSec for PI and PD atmosphere. Row 2 and 3 show the difference between OsloAeroSec and OsloAero$_{imp}$ and OsloAero$_{def}$ respectively. Dots are included in the plots to indicate where the difference between the two models is significant with a two-tailed paired Student's t–test with 95 % confidence interval.

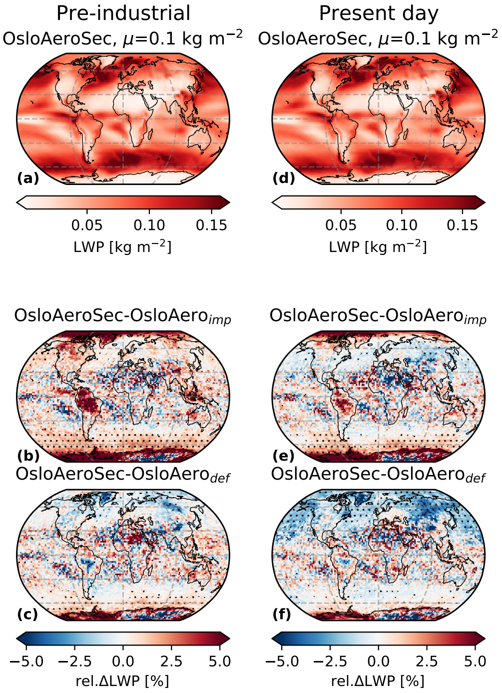

Figure S13. Top row: Liquid water path (LWP) OsloAeroSec for PI and PD atmosphere. Row 2 and 3 show the difference between OsloAeroSec and OsloAero$_{imp}$ and OsloAero$_{def}$ respectively. Dots are included in the plots to indicate where the difference between the two models is significant with a two-tailed paired Student's t–test with 95 % confidence interval.

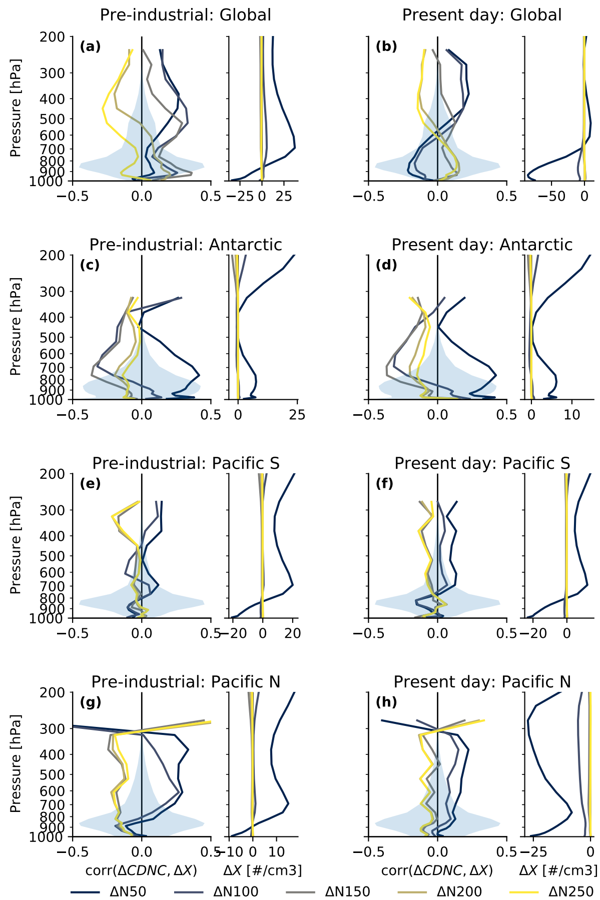

Figure S14. Left panel of each subplot: Correlations by pressure level between the change between OsloAero$_{def}$ and OsloAeroSec in cloud droplet number concentration (ΔCDNC) and the change in number of particles above 50, 100, 150,200 and 250 nm for different regions. The blue shaded signifies the relative fractional occurrence of liquid cloud and is included to give an idea of where the aerosols may actually have a noticeable impact on clouds. The right panel of each subplot shows the change in the aerosol concentration for the relevant region.

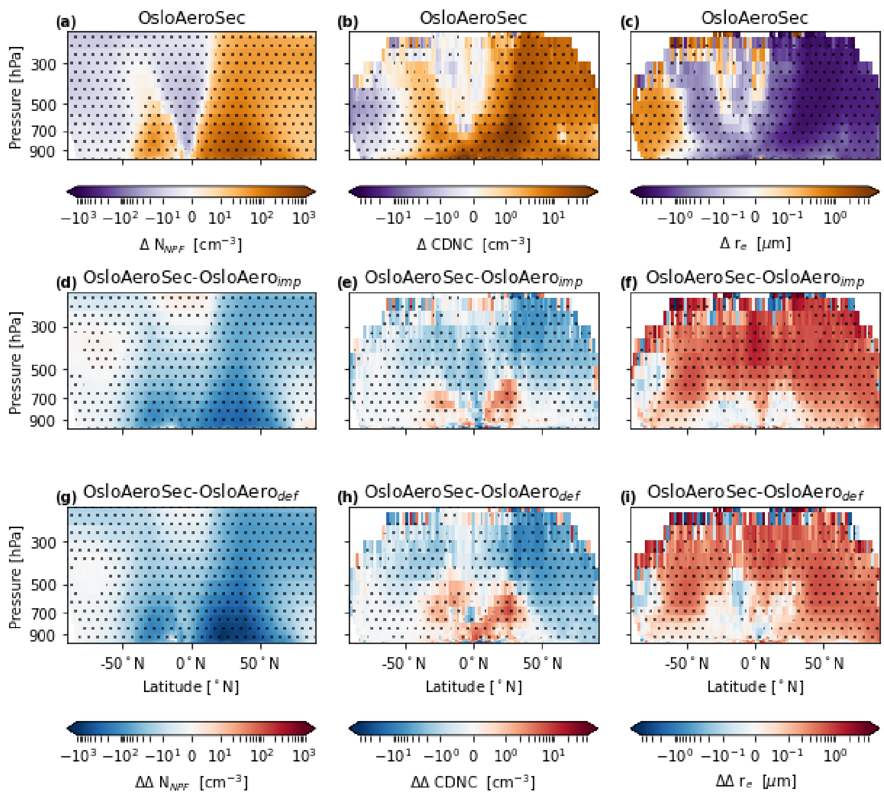

Figure S15. Zonally averaged values for N_{NPF}, cloud droplet number concentration (CDNC) and effective droplet radius (r_e). The top panel shows the PD - PI for OsloAeroSec while the second and third row shows the of this value to the value with OsloAero$_{imp}$ (second row) and OsloAero$_{def}$ (third row). Dots are included in the plots to indicate where the difference between the two models is significant with a two-tailed paired Student's t–test with 95 % confidence interval.

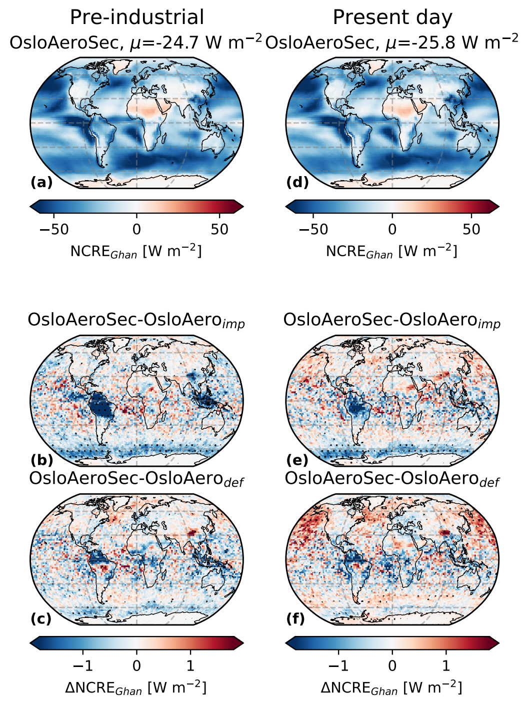

Figure S16. Top row: NCRE$_{Ghan}$ in OsloAeroSec for PI and PD atmosphere. Row 2 and 3 show the difference between OsloAeroSec and OsloAero$_{imp}$ and OsloAero$_{def}$ respectively. Dots are included in the plots to indicate where the difference between the two models is significant with a two-tailed paired Student's t–test with 95 % confidence interval.

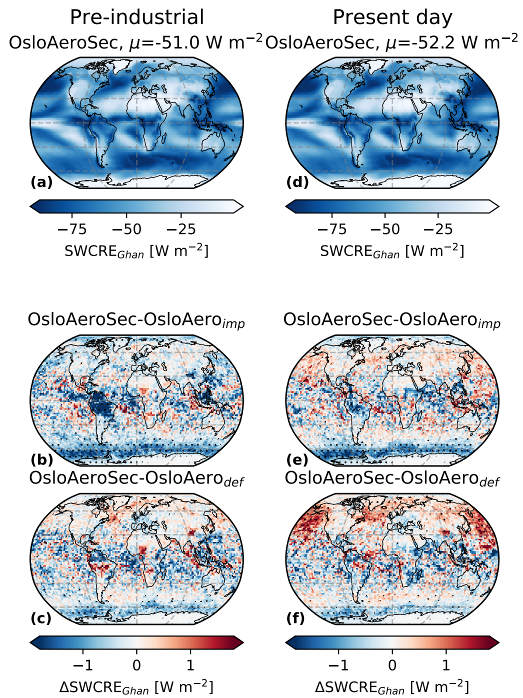

Figure S17. Top row: Short wave CRE in OsloAeroSec for PI and PD atmosphere. Row 2 and 3 show the difference between OsloAeroSec and OsloAero$_{imp}$ and OsloAero$_{def}$ respectively. Dots are included in the plots to indicate where the difference between the two models is significant with a two-tailed paired Student's t–test with 95 % confidence interval.

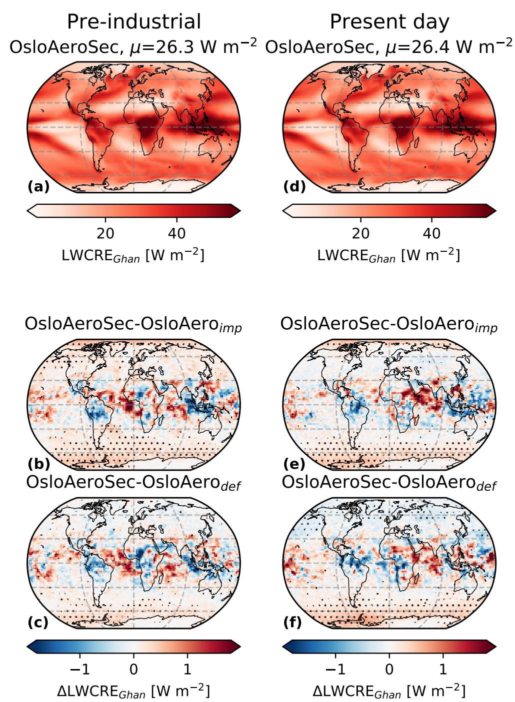

Figure S18. Top row: Long wave CRE in OsloAeroSec for PI and PD atmosphere. Row 2 and 3 show the difference between OsloAeroSec and OsloAero$_{imp}$ and OsloAero$_{def}$ respectively. Dots are included in the plots to indicate where the difference between the two models is significant with a two-tailed paired Student's t–test with 95 % confidence interval.

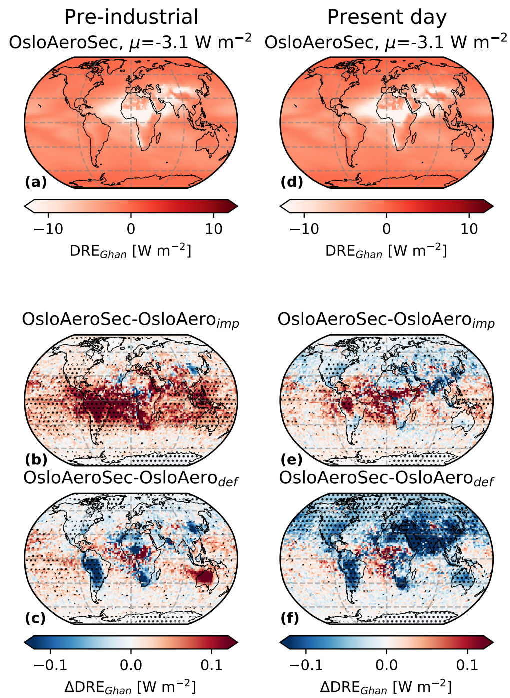

Figure S19. Top row: The direct radiative effect in OsloAeroSec for PI and PD atmosphere. Row 2 and 3 show the difference between OsloAeroSec and OsloAero$_{imp}$ and OsloAero$_{def}$ respectively. Dots are included in the plots to indicate where the difference between the two models is significant with a two-tailed paired Student's t–test with 95 % confidence interval.

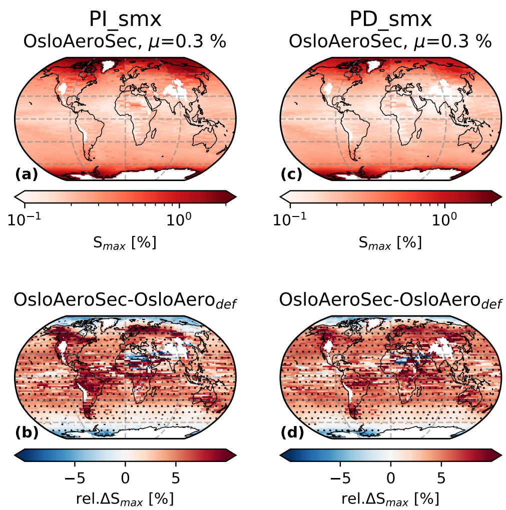

Figure S20. Top row:Average values of maximum supersaturation (S_{max}) for OsloAeroSec for PI (left) and PD (right). Row 2–3: the relative difference between OsloAeroSec and OsloAero$_{imp}$ (row 2) and OsloAero$_{def}$ (row 3) for PI (left) and PD(right). All values are averaged up to 850 hPa and weighted by pressure difference of the grid cell. Furthermore, only values where S_{max} is larger than zero are counted towards the average. Dots are included in the plots to indicate where the difference between the two models is significant with a two-tailed paired Student's t–test with 95 $\%$ confidence interval.

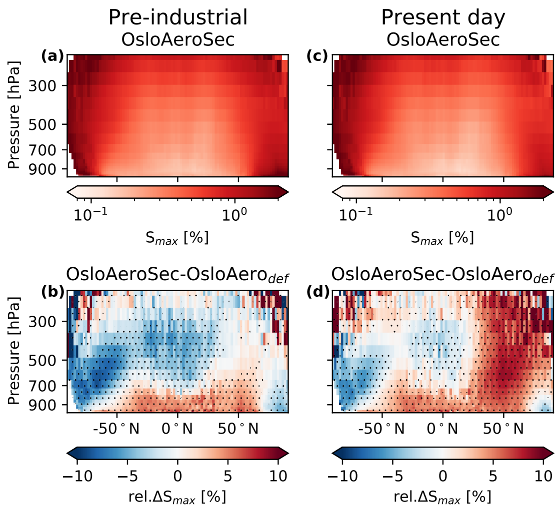

Figure S21. Top row:Average values of maximum supersaturation (S_{max} for OsloAeroSec for PI (left) and PD (right). Bottom row: the relative difference between OsloAeroSec and OsloAero$_{def}$ for PI (left) and PD(right). Only values where S_{max} is larger than zero are counted towards the average. Dots are included in the plots to indicate where the difference between the two models is significant with a two-tailed paired Student's t–test with 95 % confidence interval.

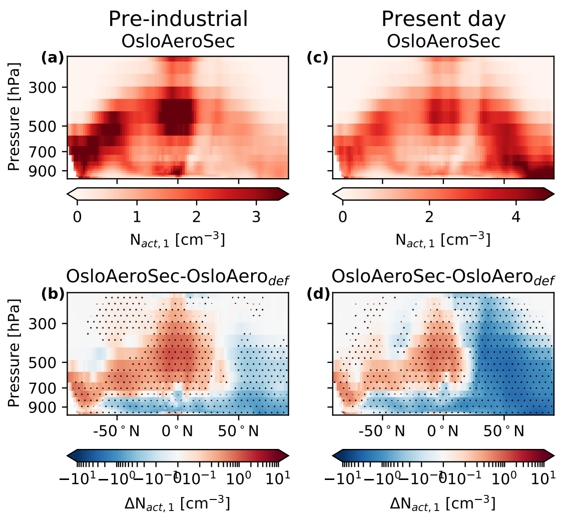

Figure S22. Top row: Average values of the averaged activation of particles from the NPF mode (mix number 1) for OsloAeroSec for PI (left) and PD (right). Bottom row: the relative difference between OsloAeroSec and OsloAero$_{def}$ for PI (left) and PD(right). The values are an approximation in the sense that they are calculated by multiplying the separately calculated monthly mean output of the number concentration in the mode and the activation fraction from that mode (see Fig. S24). Dots are included in the plots to indicate where the difference between the two models is significant with a two-tailed paired Student's t–test with 95 % confidence interval.

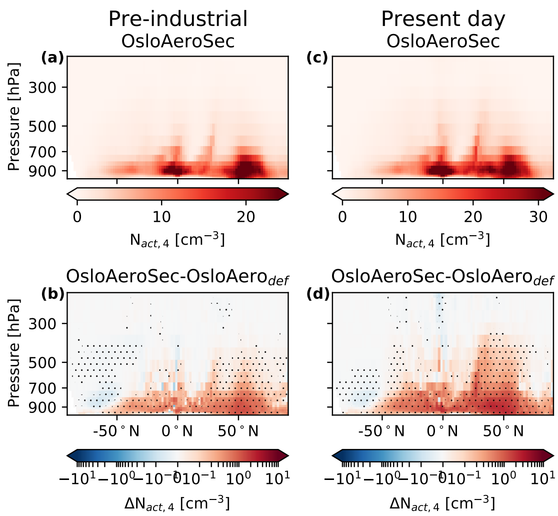

Figure S23. Top row: Average values of the averaged activation of particles from mode number 4 (mix number 4) for OsloAeroSec for PI (left) and PD (right). Bottom row: the relative difference between OsloAeroSec and OsloAero$_{def}$ for PI (left) and PD(right). The values are an approximation in the sense that they are calculated by multiplying the separately calculated monthly mean output of the number concentration in the mode and the activation fraction from that mode (see Fig. S25). Dots are included in the plots to indicate where the difference between the two models is significant with a two-tailed paired Student's t–test with 95 % confidence interval.

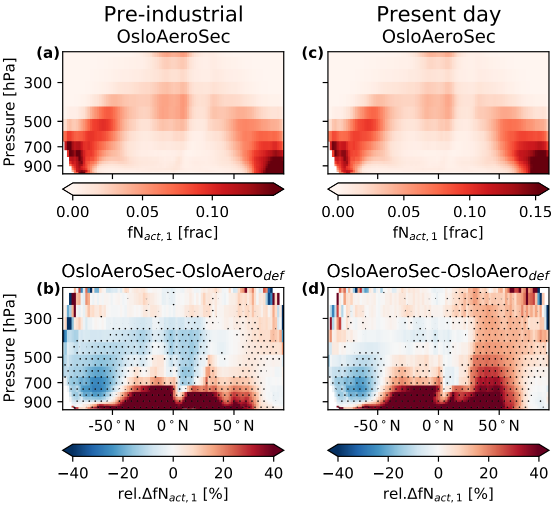

Figure S24. Top row: Average values of the activated fraction of particles from the NPF mode (mix number 1) for OsloAeroSec for PI (left) and PD (right). Bottom row: the relative difference between OsloAeroSec and OsloAero$_{def}$ for PI (left) and PD(right). The values are an approximation in the sense that they are calculated by multiplying the separately calculated monthly mean output of the number concentration in the mode and the activation fraction from that mode. Dots are included in the plots to indicate where the difference between the two models is significant with a two-tailed paired Student's t–test with 95 % confidence interval.

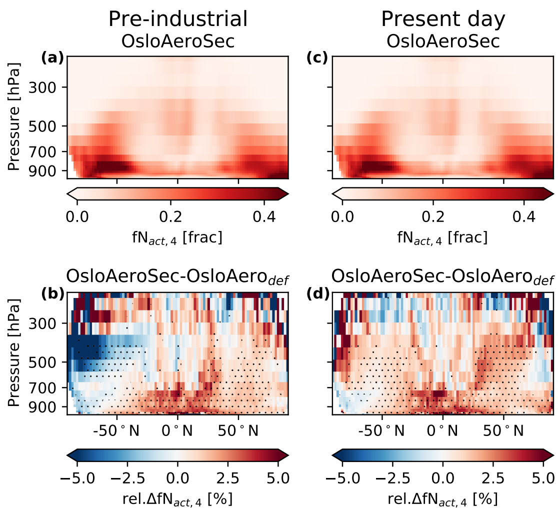

Figure S25. Top row: Average values of the activated fraction of particles from mode number 4 (mix number 4) for OsloAeroSec for PI (left) and PD (right). Bottom row: the relative difference between OsloAeroSec and OsloAero$_{def}$ for PI (left) and PD(right). Dots are included in the plots to indicate where the difference between the two models is significant with a two-tailed paired Student's t–test with 95 % confidence interval.

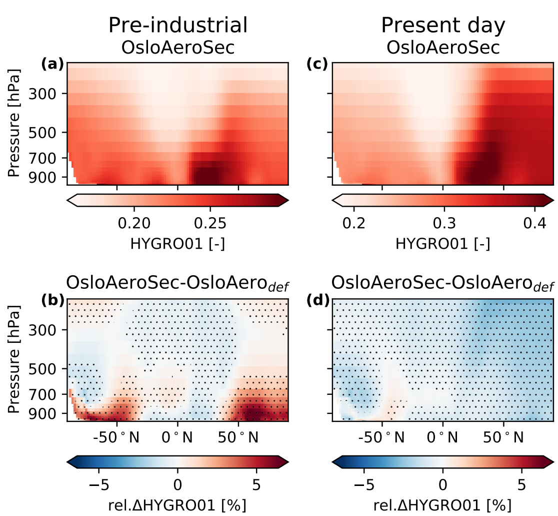

Figure S26. Top row: Average values of the hygroscopicity particles from mode number 1 (mix number 1) for OsloAeroSec for PI (left) and PD (right). Bottom row: the relative difference between OsloAeroSec and OsloAero$_{def}$ for PI (left) and PD(right). Dots are included in the plots to indicate where the difference between the two models is significant with a two-tailed paired Student's t–test with 95 % confidence interval.

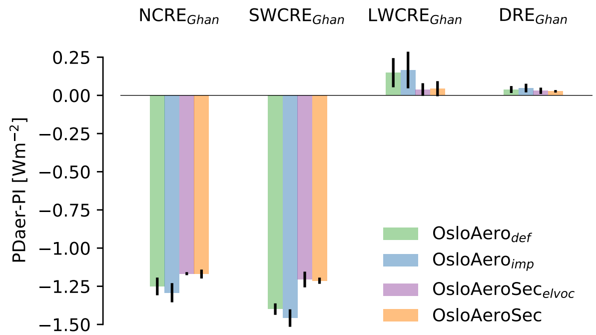

Figure S27. Globally averaged ERF for 1 year (plus one spin-up year) of simulations. The OsloAeroSec$_{elvoc}$ case is a sensitivity simulation were only 50% of ELVOC is allowed to condense onto the particles in the sectional scheme. The simulation was run to test the influence of this factor on the overall results in the paper.

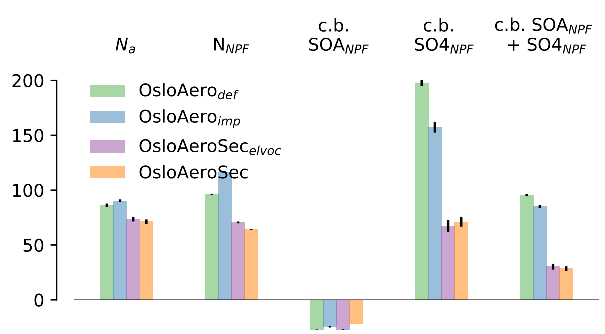

Figure S28. Globally averaged aerosol properties for 1 year (plus one spin-up year) of simulations. The OsloAeroSec$_{elvoc}$ case is a sensitivity simulation were only 50% of ELVOC is allowed to condense onto the particles in the sectional scheme. The simulation was run to test the influence of this factor on the overall results in the paper.

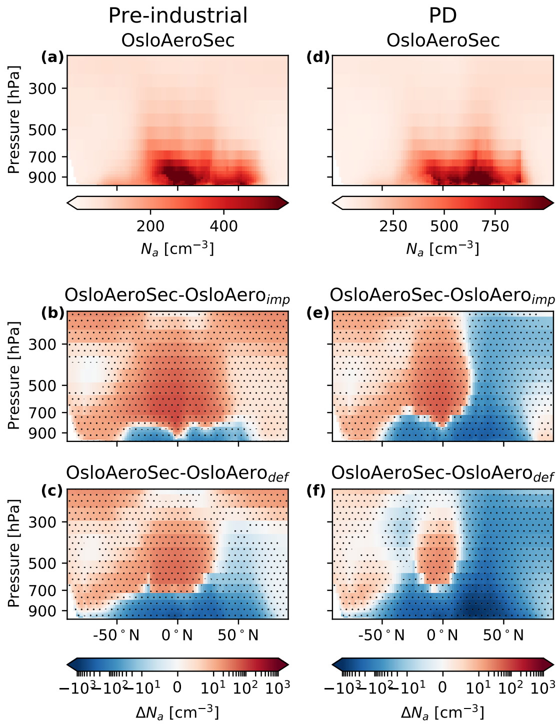

Figure S29. Zonally averaged values for N_a. The top panel shows the absolute values in the Pre-industrial (left) and Present day (right) atmosphere) PD - PI for OsloAeroSec while the second and third row shows the of this value to the value with OsloAero$_{imp}$ (second row) and OsloAero$_{def}$ (third row). Dots are included in the plots to indicate where the difference between the two models is significant with a two-tailed paired Student's t–test with 95 % confidence interval.

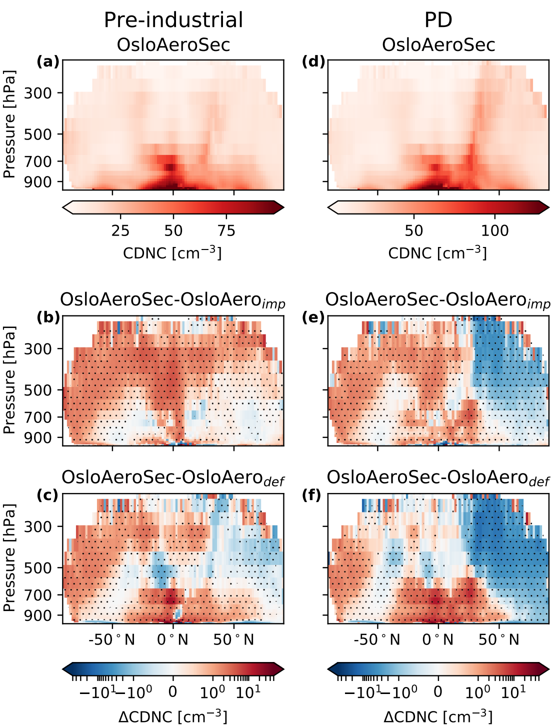

Figure S30. Zonally averaged values for cloud droplet number concentrations. The top panel shows the absolute values in the Pre-industrial (left) and Present day (right) atmosphere) PD - PI for OsloAeroSec while the second and third row shows the of this value to the value with OsloAero$_{imp}$ (second row) and OsloAero$_{def}$ (third row). Dots are included in the plots to indicate where the difference between the two models is significant with a two-tailed paired Student's t–test with 95 % confidence interval.